Materials Today Physics 22 (2022) 100601

Contents lists available at ScienceDirect

Materials Today Physics

journal homepage: https://www.journals.elsevier.com/materials-today-physics

Negligible contribution of inter-dot coherent modes to heat conduction in quantum-dot superlattice

Cheng Shao, Junichiro Shiomi*

Department of Mechanical Engineering, The University of Tokyo, 7-3-1 Hongo, Bunkyo, Tokyo, 113-8656, Japan

ARTICLE INFO

Article history:
Received 22 October 2021
Received in revised form
8 December 2021
Accepted 24 December 2021
Available online 30 December 2021

Keywords:
PbS quantum dots superlattice
Phonon engineering
Inter-dot coherence
Confinement-induced localization
Amorphous-like temperature dependence

ABSTRACT

Colloidal quantum dots (QDs) superlattice, which is made of inorganic cores and can self-assemble into various types of lattice structures, finds promising applications in optical, electrical, and optoelectronic devices. Recent inelastic neutron scattering measurement [NAT. COMMUN. 10:4236 (2019)] showed that the inter-quantum-dot vibrational frequencies can be tuned by varying the QDs shapes and ligand types, suggesting that the QDs superlattices can be a platform for phonon engineering. In this work, we quantify the impact of the second periodicity on thermal transport through full-scale molecular dynamics simulations of PbS QDs superlattice with realistic QD size and ligand morphology. The vibrational pattern analysis reveals that the vibrations can be classified into the inter-QDs coherent modes and the spatially localized modes arising from the geometry confinement. The spectral analysis indicates that spatially localized modes in the frequency range of 0.8–5 THz dominate the thermal transport and lead to an amorphous-like temperature dependence between 200 and 400 K. On the other hand, the inter-QDs coherent modes, albeit have an averaged relaxation of 10 ps, have a limited thermal conductivity value of 0.01 W/mK at room temperature due to the scarce of the vibrational states. We demonstrate that controlling the ligand morphology is more efficient than tuning the second periodicity in engineering the thermal conductivity of QDs superlattice.

1. Introduction

Colloidal quantum dots (QDs) superlattice can be synthesized from a solution of nanometer-sized inorganic particles and self-assembled into densely packed bulk materials with long-range periodicity [1,2]. The tunability ranges from the atomic composition to the size and shape, and the surface functionalization of the QDs have made them promising in a wide spectrum of applications including QDs-based solar cells [3,4], photodetectors [5], light-emitting diodes [6,7], among many others. For instance, the optical properties of lead sulfide (PbS) QDs are size dependent [8]. The energy levels of PbS QDs can be modified through the ligand exchange process [9]. The hole mobility in PbS QD thin film devices can also exhibit an orders-of-magnitude enhancement at an optimized combination of solvent and ligands during the synthesis process [10,11]. Photon detectors based on PbS QDs have also been shown with enhanced efficiency [12–14].

The thermal properties of the QDs superlattice are equally important, but less understood compared to the electrical and optical properties. Recently, Ong et al. have performed the first measurement on the thermal conductivity of the nanocrystal superlattice and found that it is in the range of 0.1–0.3 W/mK, mediated by the atomic density contrast and the chemistry at the organic/inorganic interface [15]. By systematically varying the factors like the ligand types and lengths, binding strength, and the QD diameter, Liu et al. have shown that the thermal conductivity of the QDs superlattice can be varied in the range of 0.1–0.4 W/mK [16]. More recently, Wang et al. demonstrated that the thermal conductivity of the QDs SL can be boosted by crosslinking the ligands by strong covalent bonding, which can leverage thermal conductivity to 1.7 W/mK [17].

The second periodicity of the QDs superlattice gives rise to additional types of vibrations that stem from the relative vibrations among the QDs, which we refer as inter-dot coherent phonon [18,19]. Engineering the propagation of the inter-dot coherent phonon may give us another degree of freedom to tune its thermal properties. The properties of the coherent phonon that extends over nanostructure periodicities have been well studied in structures like superlattices and phononic crystals [20–23]. As for the

* Corresponding author.
E-mail address: shiomi@photon.t.u-tokyo.ac.jp (J. Shiomi).

https://doi.org/10.1016/j.mtphys.2021.100601
2542-5293/

QDs superlattice, there are recent experimental and numerical efforts to understand its properties [24–26]. Through inelastic neutron scattering measurement and modeling, Yazdani et al. found that the phononic properties of the quantum dot system can be engineered through the constituent material of the QD cores, the surface morphology, and the ligand types [25]. Mork et al. demonstrated the tunability of the acoustic phonon frequency in colloidal nanocrystal by appropriate choice of the surface ligands [26]. However, those studies can only probe the lattice vibrational frequency of the inter-dot coherent phonon, while its contribution to thermal transport remains unknown.

On the other hand, knowing the roles of the second periodicity on heat transport in the QDs superlattice system as well as how much heat is carried by the low frequency inter-dot coherent modes is particularly important for phonon engineering. Compared with the traditional superlattice, the QDs superlattice is featured by a few characters: 1) different QDs core can exhibit different orientations, 2) the QDs are passivated by organic ligands with random orientations and distribution in the locations, and 3) the QDs are not directly connected but instead connected through the soft ligands, which gives rise to the geometry confinement of the QD cores. These features make it difficult to apply the well-developed anharmonic lattice dynamics calculation for such system [27–29].

In this work, we applied molecular dynamics (MD) simulations to directly probe the thermal transport in the PbS QDs system due to lattice vibrations. The lifetimes of the coherent phonons are calculated from the spectral energy density based on the velocity trajectories of the QDs from the MD simulations. The overall thermal conductivity is predicted from the Green-Kubo methods, and the atomic-level information is revealed from the eigenmode and the spectral heat flux analysis. Our results suggest that although the inter-QDs coherent modes have an averaged relaxation time of 10 ps and can propagate over a few QDs, the scarce of the vibrational states limits their thermal conductivity contribution to 0.01 W/mK. Instead, the spatially localized modes, which are insensitive to the second periodicity, contribute to 80% of the total thermal conductivity (0.14 W/mK) at room temperature. We also demonstrate that controlling the ligand morphology is more effective than tunning the second periodicity in engineering the thermal conductivity of QDs superlattice.

2. Results

We firstly look at the phonon band structure of the PbS QDs superlattice calculated from harmonic lattice dynamics [23]. Fig. 1(a) is the phonon dispersion relations in the full frequency range, while Fig. 1(b) shows the zoomed-in dispersion in the low frequency range. We observed dense vibrations at frequency less than 12 THz with a gap at around 8 THz, followed by discretized vibrations in the frequency range of 17–24 THz. As the maximum vibrational frequency allowed in bulk PbS is around 12 THz, we mainly attribute these dense vibrations below 12 THz to the atomic vibrations in the PbS core. On the other hand, the high-frequency modes in the range of 17–24 THz are mainly contributed by the stiff C–C bonds in the ligands [15]. From the dispersion relations, most of the bands are flattened and separated by mini gaps, indicating that they are standing waves with negligible group velocities. Such characteristics usually lead to the low thermal conductivity of a material [31]. Two mechanisms can be responsible for the band flatten: 1) the interference of the phonons that reflect from multiple interfaces, and 2) the geometry confinement of the QDs. Since, as we will show later, the thermal conductivity of the QDs system is insensitive to the variation in the size of the QDs core, we associate the band flattening and the reduction in the group

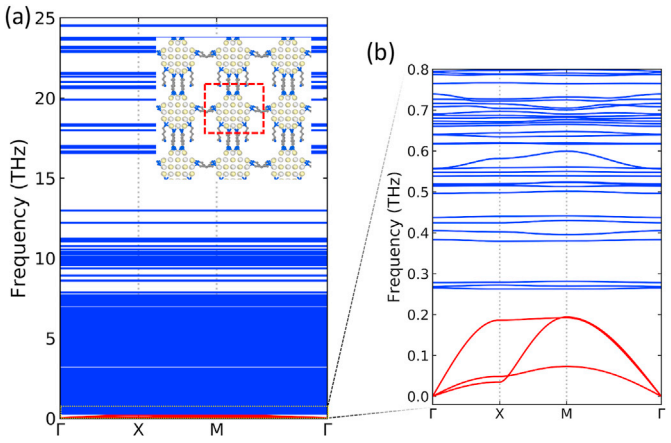

Fig. 1. Phonon band structure of PbS QDs superlattice calculated from the harmonic lattice dynamic. (a) phonon dispersion in the full frequency range, and (b) phonon dispersion in the low frequency range. The inset in the (a) shows the structure of the QDs used for the calculation, which contains 185 atoms in each QD.

velocities to the geometry confinement effect. It is worth noting that the three acoustic branches, marked in red in Fig. 1(a) and (b), show notable dispersion and group velocities. In the following sections, we will show that those three branches are related to inter-QDs coherent modes. Overall, our phonon dispersion is similar to that found in gold nanocrystal superlattice [32].

Before getting into the thermal conductivity calculation, we analyze the characteristics of vibrational modes in the system. Phonon participation ratio (PR) is a good measure of the extension of the vibrations modes [33]. It has severed as a criterion to separate the diffusions and locons in amorphous materials [34] and has also been used as a signature of the Anderson localization in the multilayer structure [35]. The average phonon PRs in the frequency range of 0–25 THz are shown in Fig. 2(a). One can see that the PR in the system is in general less than 0.2 when the frequency is larger than 2 THz. Such low PRs suggest that the majority of the vibrations are either localized inside the QDs or in the ligands. Fig. 2(b) and (c) show two representative vibrational modes in this system. For vibrational modes with a large PR (Fig. 2(b)), all atoms participated in the vibrations, which is a signature of the inter-QD modes. On the other hand, for modes with small PR values (Fig. 2(c)), only part of the atoms participate in the vibrations, suggesting a localization. The modes with large PRs are related to the low-lying acoustic modes in the dispersion relations as shown in Fig. 1(b).

We next study the contribution of the inter-QDs coherent modes to thermal transport. According to the linearized Boltzmann transport of phonon gas, the thermal conductivity can be written as the summation of different vibrational modes as $k = \frac{1}{3}\sum_{\omega} c_{\omega} v_{\omega}^2 \tau_{\omega}$, where c_{ω}, v_{ω}, τ_{ω} are the heat capacity, group velocity, and the relaxation time of phonon mode with frequency ω. To probe the lifetimes of the coherent modes, we took the spectral energy density (SED) analysis approach [36,37]. The structure used for the spectral energy analysis is shown in Fig. 3(a), which contains $20 \times 3 \times 3$ QDs, and are packed in a simple cubic lattice structure [38]. Note that although the atoms inside each QD have a well-defined lattice structure, the perturbation on the ligand location as well as the randomness in ligand orientations make the normal mode projection, which is an alternative method to extract modal lifetime, tricky [39]. Besides, different QDs can have different orientations at room temperature due to thermal fluctuation. We firstly tried to explicitly consider all the internal atomic vibrations in the QDs and the ligands and project them to the reciprocal lattice

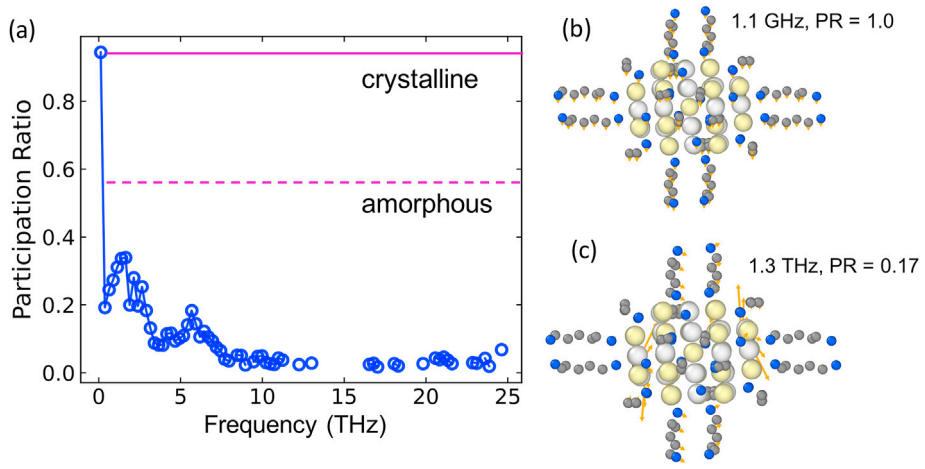

Fig. 2. (a)The averaged participation ratio (PR) in the PbS QDs as a function of frequency. The horizontal lines represent the typical PRs in crystalline and amorphous materials. (b) Illustration of the inter-QD transverse acoustic vibration mode. In this mode, all atoms are moved in the direction perpendicular to the wavevector, and the atomic displacements are the same. The frequency of this mode is 1.1 GHz, and the PR is 1.0. (c) Another mode at frequency of 1.3 THz. In this mode, part of the vibrations are localized inside the QD and part of the vibrations are localized in the ligands.

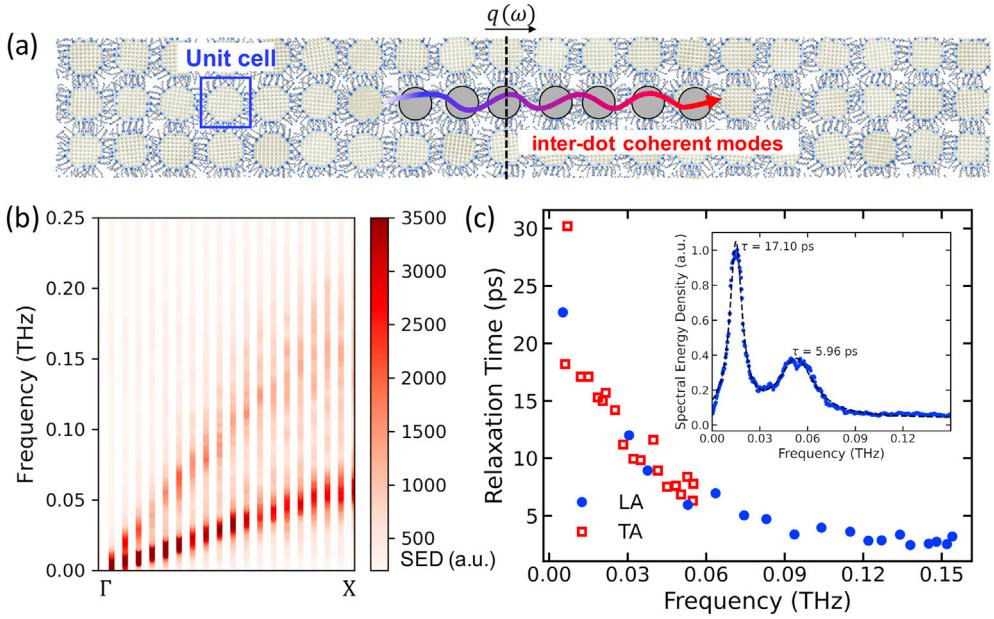

Fig. 3. (a) Illustration of the system used for the spectral energy density (SED) analysis. The horizontal dashed line represents the interface used for the spectral heat flux calculation (b) The spectral energy density calculated from the center-of-mass (COM) velocities of the QDs along the Γ to X direction. (c) The relaxation times of the inter-QDs coherent modes extracted from the linewidths of the SED. The red open square represents the transverse acoustic (TA) modes and the blue solid dot represent the longitudinal acoustic (LA) modes. The inset of figure (c) shows the fitting of the SED with a double-Lorentzian function, and the relaxation times are extracted from the full width at half maximum of the Lorentzian peaks.

vector of the QD superlattice. However, due to the large number of atoms in a unit cell, the SED contour becomes blurred, which makes it difficult to extract any useful linewidth information.

Therefore, given the fact that the coherent phonons are the vibrations among the QDs, where the atoms inside each QDs vibrate collectively, we can also treat each QD as a super-atom, and project its center-of-mass (COM) velocity to the lattice structure of the superlattice. The resulting spectral energy density along the path from Γ to *X* at 300 K is shown in Fig. 3(b). The two explicit lines seen in the SED color contours represent the longitudinal acoustic (LA) and transverse acoustic (TA) coherent modes. Based on the linewidths, we extract the phonon lifetimes, and the results are shown in Fig. 3(c). The lifetimes are in the range of 5−30 ps and show an exponential decay trend with frequency. The LA-polarized modes have an averaged relaxation time of 5.5 ps, while for TA-polarized modes the averaged relaxation time is 12.6 ps. From the dispersion relations in Fig. 3(b), we also estimated the group velocity of the transverse and longitudinal inter-QD coherent modes to be 550 and 1230 m/s. In combination with the lifetimes from Fig. 3(c), we estimated that the mean free paths of the coherent modes are on the order of 10 nm, which spans multiple inter-QDs distances. Note that a much larger supercell structure is required to calculate the lifetimes along other symmetry paths, which is beyond our computational limit [40]. We thus adopted the isotropic assumption and estimated the contribution of the inter-QDs coherent phonon to the thermal conductivity to be less than 0.01 W/mK

[41,42]. Such small contribution of the inter-QD coherent modes is mainly due to the factor that the density-of-state of such modes (equals to $3N_{QD}$, where N_{QD} is the number of QDs, and each QD contains 485 atoms) is quite small compared to the total density of states available in the system (equal to $3N_{atom}$, where N_{atom} is the total number of atoms).

The above analysis has shown that the inter-QDs coherent modes have a quite limited contribution (0.01 W/mK) to the total thermal conductivity (0.14 W/mK as we will show later). Therefore, even though the recent studies have demonstrated that the inter-QDs vibrational frequencies can be tuned by varying the QDs shapes and ligand types, the room for engineering the thermal conductivity of the QDs superlattice by manipulating the coherent modes is limited as their contribution to thermal conductivity are small [43,44].

The above discussions mainly focused on the contribution of the inter-QD coherent modes. To gain more insights on thermal transport, we also calculate the overall thermal conductivity of the QD superlattice by the Green-Kubo method. The size-dependent thermal conductivity contains enriching information on the mean free paths of the underlying heat carriers [45,46]. We first check the size effect by calculating the thermal conductivities of a series of systems with 3×3×3, 4×4×4, 5×5×5, and 6×6×6 QDs unit cells. For each system, fifteen independent simulations with different initial velocities were used to sample the phase space. A typical example of the integral of the heat current autocorrelation function (HCACF) is shown in Fig. S3 of the Supplementary Data (SD). We observed large oscillations in the integral of the HCACF, with the oscillation frequency inverse proportional to the QDs size. Dividing the size of the QDs by the oscillation period yields a velocity of 2790 m/s, which falls between the speed of transverse (1850 m/s) and longitudinal (4100 m/s) long wavelength phonons in bulk PbS [47]. The similarity between the oscillation velocity and the speed of long wavelength modes in PbS suggests that the oscillation results from the multiple reflections of the long-wavelength acoustic modes inside the QDs. The thermal conductivities of 3×3×3, 4×4×4, 5×5×5, and 6×6×6 QDs superlattices are shown in Fig. S4 of the SD. The values fall within the error bars, indicating a size-independence of thermal conductivity. A previous study on gold nanocrystal also found a converged thermal conductivity with a system size down to 2×2×2 QDs [24]. Note that modes with wavelength larger than the side length of the simulation box cannot exist in a periodic system [48]. The weak system-size dependence also suggests that the contribution of the inter-QDs mode with wavelength larger than 3 times the inter-QD distance is negligible. This finding is consistent with the estimation that the contribution of the inter-QDs coherent modes to thermal conductivity is less than 0.01 W/mK. In the following section, we use a 3×3×3 QDs supercell system for the Green-Kubo calculation to reduce the computational costs.

To understand the origin of the localization (Fig. 2(a)), we consider three types of systems here: 1) QDs with uniform size (all the PbS QDs contains 485 atoms in the core), 2) QDs with small size difference (a binary mixing of QDs with 485 and 365 atoms in the core), and 3) QDs with large size difference (a binary mixing of QDs with 485 and 261 atoms in the core). The snapshots of those three systems are shown in Fig. 4(a). The total thermal conductivity is more sensitive to variation in the size of QDs if the localization is originated from the interference effect; in contrast, the confinement induced localization is more robust to the variation in the QDs size [49,50]. Note that the QDs superlattice with controllable size variation has also been synthesized recently [51]. The thermal conductivities of the QDs superlattice at the temperature range of 50–400 K are shown in Fig. 4(b). Regardless of the variation in the QDs sizes, the thermal conductivities of those three systems fall

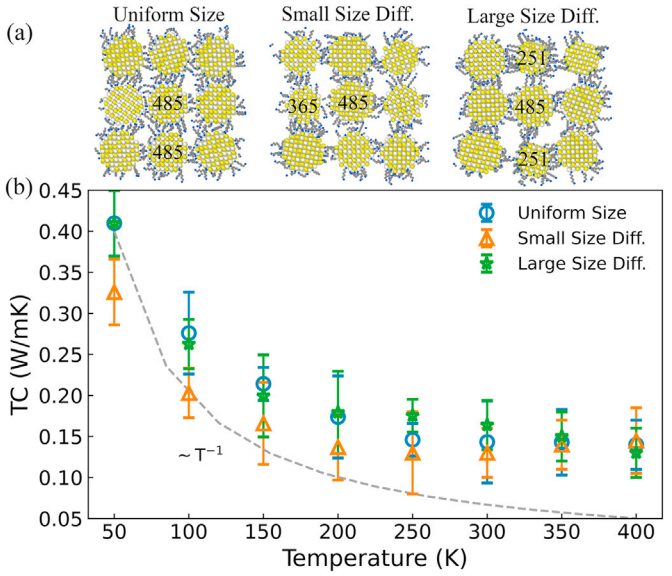

Fig. 4. (a) Illustration of QD superlattice with different degree of size variation. From left to right are: QDs with uniform size, QDs with small size variation, and QDs with large size variation. The number on the QDs represent the number of atoms in the QD core. (b)The thermal conductivity of the QDs superlattice in the temperature range of 50–400 K.

within the error bars. In the low temperature range, the thermal conductivity decays from 0.35 W/mK to 0.14 W/mK as the temperature increases from 50 to 200 K. The decay rate is slower than T^{-1} dependence typically found in crystals. At higher temperature range between 200 and 400 K, the thermal conductivity shows an amorphous-like temperature dependence. The robustness of the thermal conductivity to the variation in the QDs size suggests that the inter-QDs localization arises from the geometry confinement effect.

To gain a deeper insight into the thermal transport in the QD superlattice, we also calculate the frequency-resolved thermal conductivity accumulation function from the cross-correlation of the Fourier transformed velocities and forces, and the results are shown in Fig. 5(a). The cumulative thermal conductivity of bulk PbS is also shown in Fig. 5(a) for comparison. Phonons in the frequency range of 0.8–5 THz contribute to 80% of the total thermal conductivity in PbS QDs superlattice and the thermal conductivity exhibits a large reduction from the bulk PbS in the same frequency range. Fig. 5(b) shows the various vibrational density of state (DOS) in the QDs superlattice system: namely the atomic vibration in the QD core, the atomic vibration in the ligand, the center-of-mass (COM) vibration of the QDs, and the COM vibration of the ligands. The center-of-mass DOSs of QDs and ligands are calculated from their corresponding center-of-mass velocities and show single peaks in the low-frequency range. In contrast, the atomic vibrations are calculated from the atomic velocities of atoms inside the QDs and the ligands, and those atoms are connected by strong ionic and covalent bonds. Thus, the atomic DOSs exhibit much larger vibrational frequencies. The large overlapping between the atomic vibration of PbS and ligands in the same frequency range of 0.8–5 THz indicates that heat is diffusively transported among the localized vibrations in the QDs superlattice, which also supports the amorphous-like temperature dependence in Fig. 4(b).

Given that the coherent modes have limited contribution to thermal transport, a meaningful question should be if there are other factors that can be utilized to tune its thermal properties. Here, we also study the dependence of thermal conductivity on the

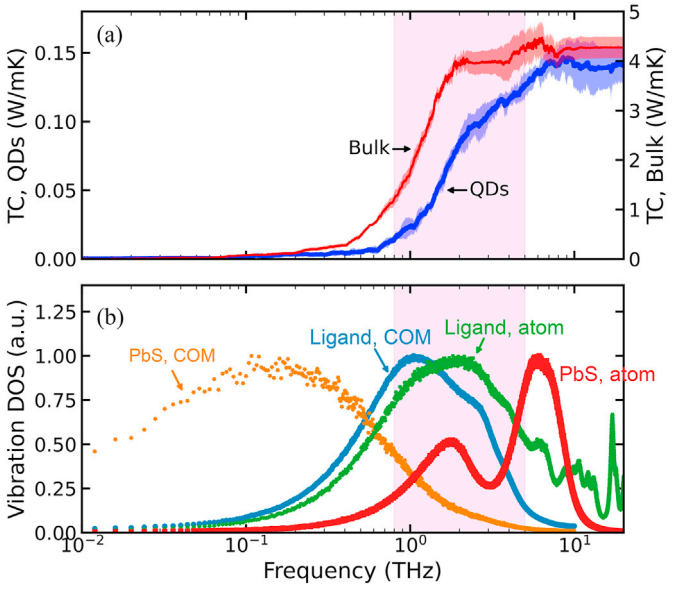

Fig. 5. (a) The cumulative thermal conductivity in the QDs SL with uniform size distribution (blue) and in bulk PbS (red) at temperature of 300 K. (b) The vibrational density of state (DOS) that breakdown into the PbS center-of-mass (COM), the ligand COM, the atomic vibrations in PbS QD (PbS, atom), and the atomic vibrations in the ligand (Ligand, atom).

ligand coverage ratios. The thermal conductivities at different ligand coverage ratios are shown in Fig. 6(b). As the ligand coverage ratio increases, the thermal conductivity firstly decreases and then increases with the ligand coverage ratio. The corresponding structures at different ligand coverage ratios are shown in Fig. 6(a). In the low ligand coverage ratio, the quantum dots connect to each other (fusion). As the ligand's coverage ratio increases, the quantum dots disconnect from each other and thus lead to a reduction in the effective binding energy of the direct QDs connection. However, further increasing the ligand coverage ratio strengthens the indirect connection between QDs through the ligands. The detailed binding energies at different ligand coverage ratios are shown in Fig. S5 of the SD. This highlights the competing effect between the fusion and the increase in binding energy and suggests that controlling the ligand morphology is an effective way to tune the thermal conductivity of QDs superlattice.

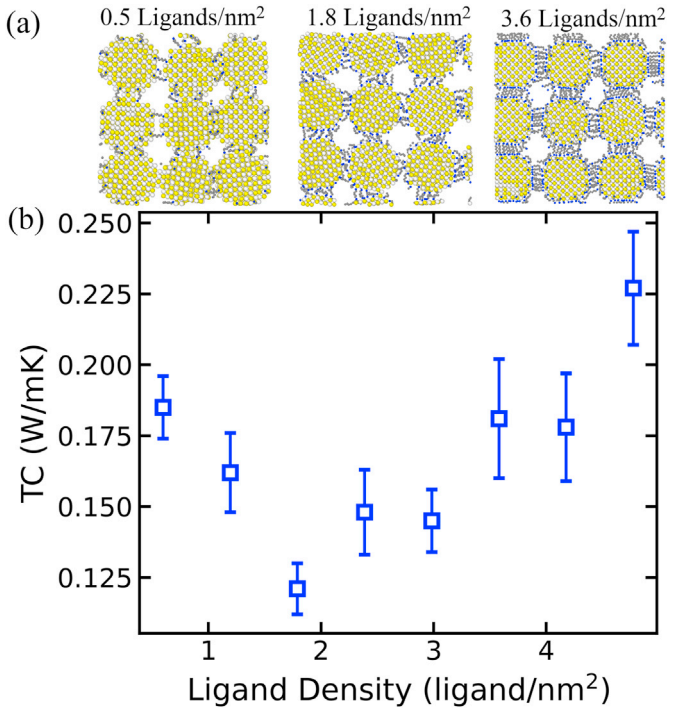

Fig. 6. (a) Snapshots of the QDs superlattice at different ligand coverage ratio. (b) Thermal conductivity of PbS QDs at different ligands coverage ratio.

3. Summary

In conclusion, we investigated the thermal transport in the PbS QDs superlattice using molecular dynamics simulations. We have identified the relaxation time of the inter-QDs coherent modes in a typical QDs superlattice to be the order of 10 ps. The scarce of the vibrational density of the inter-QDs coherent modes limit their contribution to thermal conductivity to 0.01 W/mK at room temperature, which is negligible compared to the total thermal conductivity of 0.14 W/mK. On the other hand, the eigenvector and PR analysis suggest that the majority of the vibrations are localized in the QDs and ligands and conduct heat diffusively, which manifest itself in the amorphous-like temperature dependence between 200 and 400 K. The QDs-size-insensitive thermal conductivities indicate that the spatial localization arises from the geometry confinement instead of the interference effect. We also highlight the importance of the ligands morphology on engineering the thermal transport in the QDs superlattice system.

4. Methods

4.1. Molecular dynamics simulation

The transferable force field based on a partially charged rigid ion model is used to describe the interactions between PbS, which has the functional form of [52]

$$U_{ij} = \frac{q_i q_j}{r_{ij}} + Ae^{-r_{ij}/\rho} - \frac{C_6}{r_{ij}^6} \quad (1)$$

where U_{ij} is the potential energy between atom i and j at distance of r_{ij}. q_i is the effective charge for atom i, which is $+0.8\ e$ for Pb atom and $-0.8\ e$ for S atom. The parameters A, ρ, and C are the same as those used in the reference. [52] The HS-$[CH_2]_5$-SH ligand was used to cap the QD surface. In the simulation, the light hydrogen atoms are treated implicitly with their masses lumped into the corresponding carbon atoms [53]. The force fields for ligands are adapted from Ref. [54]. The cut-off distance for Coulomb interactions and LJ potentials is set to 10 Å. A damped shifted force model with a damping constant of 0.3 $Å^{-1}$ was used to calculate the Coulomb interaction [55]. All the molecular dynamics simulations were run using LAMMPS with a timestep of 2.5 fs [60].

For harmonic lattice dynamics calculation (Figs. 1 and 2), each PbS QD contains 81 atoms and is covered by 16 ligands. For thermal conductivity calculation (Figs. 3–5), each PbS QD contains 485 atoms (diameter of 3 nm), and is covered by 74 ligands. For the ligand coverage ratio study (Fig. 6), each PbS QD is covered by 20–140 ligands. The equivalent to a ligand coverage ratios are 0.5–5 ligands/nm^2 and are similar to that found from experimental measurements and density functional calculations [56,57]. The procedures to construct the PbS QD superlattice are described in the Sec S1 of the SD.

4.2. Harmonic lattice dynamic calculation

The phonon frequency ω and eigenvector $\varepsilon(\boldsymbol{k}, \upsilon)$ are obtained by diagonalizing the dynamics matrix of the system, which is constructed from the harmonic interatomic force constants through the following equation [30]:

$$D_{3(j-1)+\alpha,3(j'-1)+\alpha'}(\boldsymbol{k}) = \frac{1}{\sqrt{m_j m_{j'}}} \sum_{l'}^{N} \frac{\partial^2 \Phi}{\partial r_\alpha \begin{pmatrix} j \\ 0 \end{pmatrix} \partial r_{\alpha'} \begin{pmatrix} j' \\ l' \end{pmatrix}} \times \exp\left(ik \cdot \left[r \begin{pmatrix} j' \\ l' \end{pmatrix} - r \begin{pmatrix} j \\ 0 \end{pmatrix} \right] \right) \quad (2)$$

where α and α' represent the cartesian directions, $\boldsymbol{k}$ is the phonon wavevector, υ is the phonon polarization index, N is the number of the unit cell in the system, and Φ is the potential energy. $r \begin{pmatrix} j \\ l \end{pmatrix}$ represents the position of the j -th atom in the l -th unit cell, and m_j is the mass of atom j. The corresponding force constants are obtained from the finite displacement method through the ALAMODE package [58].

The PR, which measures the degree of spatial localization of a vibration mode, is calculated from the following equation [33]:

$$PR = \frac{\left(\sum_i^N |\varepsilon_i(k,\upsilon)|^2 \Big/ m_i \right)^2}{N \sum_i^N \frac{|\varepsilon_i(k,\upsilon)|^4}{m_i^2}} \quad (3)$$

where N is the number of atoms in the unit cell, m_i is the mass of atom i, and $\varepsilon_i(k, \upsilon)$ eigenvector component of atom i. A PR of 1 represents a propagating mode with all atoms evolved in the vibrations. On the other hand, a small PR represents a spatially localized mode with only part of atoms involved in the vibration. In an extreme scenario, only one atom participates in the vibration, and the PR is at the order of O (1/N).

4.3. Thermal property calculation

The thermal conductivity of the QDs superlattice system is calculated from the Green-Kubo methods

$$k = \frac{1}{k_B V T^2} \int_0^\infty \frac{\langle \boldsymbol{q}(t) \cdot \boldsymbol{q}(0) \rangle}{3} dt, \quad (4)$$

where k_B is the Boltzmann constant, V is the volume of the system, T is the temperature, and $\langle \boldsymbol{q}(t) \cdot \boldsymbol{q}(0) \rangle$ is the heat current autocorrelation function (HCACF).

Prior to the heat flux calculation, the system is relaxed in an *NVE* ensemble for 10 ns. The heat flux is then collected during a time span of 2.5 ns and used for the HCACF calculation. The final HCACF and the thermal conductivity is averaged over 15 independent simulations. The typical heat current autocorrelation function and its integral thermal conductivity are shown in Fig. S3 of the SD.

The total heat flux across the system can be decomposed spectrally as [59]

$$Q = \int_0^\infty \frac{d\omega}{2\pi} q_{ij}(\omega) \quad (5)$$

where $q_{ij}(\omega)$ is the spectral heat flux between atom i and j across the interface marked on Fig. 3(a) and can be calculated from the Fourier transform of the force-velocity cross-correlation

$$q_{ij}(\omega) = \frac{2}{A} \mathrm{Re} \sum_{j \in L} \sum_{i \in R} \int_{-\infty}^{\infty} d\tau e^{i\omega\tau} \langle \boldsymbol{F}_{ij}(\tau) \cdot \boldsymbol{v}_i(0) \rangle \quad (6)$$

where A is the area of the cross-section, the angular bracket represent the cross-correlation, τ is the correlation time, $\boldsymbol{F}_{ij}$ is the force acting on atom i on the right side of the interface from atom j on the left side of the interface. For the spectral heat flux calculation, the velocity and force information are collected very 20 fs for a total time span of 2.5 ns Five independent simulations are used to obtain the averaged spectral flux. The spectral heat fluxes calculated at different locations are shown in Fig. S6 of SD.

The spectral energy density of the inter-QDs vibrations is calculated from [36,37]

$$\Phi(\boldsymbol{k}, \omega) = \frac{1}{4\pi\tau_0} \sum_\alpha^3 \frac{m_{QD}}{N_{QD}} \left| \sum_l^N \int_0^{\tau_0} \dot{u}_\alpha^l \exp\left(ik \cdot r_0^l - i\omega t \right) dt \right|^2 \quad (7)$$

where $\Phi(\boldsymbol{k}, \omega)$ is the spectral energy at wavevector $\boldsymbol{k}$ and frequency ω, τ_0 is the time duration of the Fourier transform. The α and l are the indices for the directions and QDs. m_{QD} is the total mass of each QDs and N_{QD} is the number of QDs in the supercell. $\dot{u}_\alpha^l$ is the center-of-mass velocity of l - th QD at direction α, which is obtained from the built-in command in LAMMPS [60]. The center-of-mass velocities of QDs are dumped every 20 fs for a total time span of 2.5 ns and are used for the spectral energy density calculation. The spectral energy density at a specify wavevector $\boldsymbol{k}$ can be fitted with a N-Lorentzian function of the form

$$\Phi(\boldsymbol{k}, \omega) = \sum_i^N \frac{C_i}{(\omega - \omega_i)^2 + \Gamma_i^2} \quad (8)$$

to extract the central frequency ω_i and the linewidth Γ_i of phonon mode i, and the corresponding phonon lifetime is obtained through the relation $\tau_i = 1/2\Gamma_i$.

Data availability statement

The original data in this work is available from the corresponding author upon reasonable requests.

Credit author statement

Cheng Shao: Conceptualization; Methodology; Writing. Junichiro Shiomi: Conceptualization; Supervision; Writing-Reviewing and Editing

Declaration of competing interest

The authors declare that they have no known competing financial interests or personal relationships that could have appeared to influence the work reported in this paper.

Acknowledgments

The authors would like to thank Prof. Yoshihiro Iwasa and Dr. Satria Bisri for the discussion. This study is partially supported by JSPS KAKENHI Grant No. 19H00744 from Japan Society for the Promotion of Science (JSPS) and CREST Grant No. JPMJCR19I2 from Japan Science and Technology Agency (JST). The calculations in this work were performed using supercomputer facilities of the Institute for Solid State Physics, the University of Tokyo.

Appendix A. Supplementary data

Supplementary data to this article can be found online at https://doi.org/10.1016/j.mtphys.2021.100601.

References

[1] C.B. Murray, C.R. Kagan, M.G. Bawendi, Self-organization of CdSe nanocrystallites into three-dimensional quantum dot superlattices, Science 270 (1995) 1335.
[2] K.J. Si, Y. Chen, Q. Shi, W. Cheng, Nanoparticle superlattices: the roles of soft ligands, Adv. Sci. 5 (2018) 1700179.
[3] O.E. Semonin, J.M. Luther, S. Choi, H.-Y. Chen, J. Gao, A.J. Nozik, M.C. Beard, Peak external photocurrent quantum efficiency exceeding 100% via MEG in a quantum dot solar cell, Science 334 (2011) 1530.
[4] J. Gan, M. Yu, R.L.Z. Hoye, K.P. Musselman, Y. Li, X. Liu, Y. Zheng, X. Zu, S. Li, J.L. MacManus-Driscoll, L. Qiao, Defects, photophysics and passivation in Pb-based colloidal quantum dot photovoltaics, Mater. Today Nano 13 (2021) 100101.
[5] C. Livache, B. Martinez, N. Goubet, C. Gréboval, J. Qu, A. Chu, S. Royer, S. Ithurria, M.G. Silly, B. Dubertret, E. Lhuillier, A colloidal quantum dot infrared photodetector and its use for intraband detection, Nat. Commun. 10 (2019) 2125.
[6] C.R. Kagan, E. Lifshitz, E.H. Sargent, D.V. Talapin, Building devices from colloidal quantum dots, Science 353 (2016).
[7] F.P.G. de Arquer, D.V. Talapin, V.I. Klimov, Y. Arakawa, M. Bayer, E.H. Sargent, Semiconductor quantum dots: technological progress and future challenges, Science 373 (2021).
[8] I. Moreels, K. Lambert, D. Smeets, D. De Muynck, T. Nollet, J.C. Martins, F. Vanhaecke, A. Vantomme, C. Delerue, G. Allan, Z. Hens, Size-dependent optical properties of colloidal PbS quantum dots, ACS Nano 3 (2009) 3023.
[9] P.R. Brown, D. Kim, R.R. Lunt, N. Zhao, M.G. Bawendi, J.C. Grossman, V. Bulović, Energy level modification in lead sulfide quantum dot thin films through ligand exchange, ACS Nano 8 (2014) 5863.
[10] L. Liu, S.Z. Bisri, Y. Ishida, D. Hashizume, T. Aida, Y. Iwasa, Ligand and solvent effects on hole transport in colloidal quantum dot assemblies for electronic devices, ACS Appl. Nano Mater. 1 (2018) 5217.
[11] X. Liu, P. Lu, H. Zhai, Ligand coverage dependence of structural stability and interparticle spacing of gold supracrystals, J. Appl. Phys. 123 (2018): 045101.
[12] V. Sukhovatkin, S. Hinds, L. Brzozowski, E.H. Sargent, Colloidal quantum-dot photodetectors exploiting multiexciton generation, Science 324 (2009) 1542.
[13] K. Xu, W. Zhou, Z. Ning, Integrated structure and device engineering for high performance and scalable quantum dot infrared photodetectors, Small 16 (2020) 2003397.
[14] W. Zhou, Y. Shang, F.P. García de Arquer, K. Xu, R. Wang, S. Luo, X. Xiao, X. Zhou, R. Huang, E.H. Sargent, Z. Ning, Solution-processed upconversion photodetectors based on quantum dots, Nat. Electron. 3 (2020) 251.
[15] W.-L. Ong, S.M. Rupich, D.V. Talapin, A.J.H. McGaughey, J.A. Malen, Surface chemistry mediates thermal transport in three-dimensional nanocrystal arrays, Nat. Mater. 12 (2013) 5.
[16] M. Liu, Y. Ma, R.Y. Wang, Modifying thermal transport in colloidal nanocrystal solids with surface chemistry, ACS Nano 9 (2015) 12079.
[17] Z. Wang, A.S.S. Singaravelu, R. Dai, Q. Nian, N. Chawla, R.Y. Wang, Ligand crosslinking boosts thermal transport in colloidal nanocrystal solids, Angew. Chem. Int. Ed. 59 (2020) 9556.
[18] O.L. Lazarenkova, A.A. Balandin, Miniband formation in a quantum dot crystal, J. Appl. Phys. 89 (2001) 5509.
[19] O.L. Lazarenkova, A.A. Balandin, Electron and phonon energy spectra in a three-dimensional regimented quantum dot superlattice, Phys. Rev. B 66 (2002) 245319.
[20] M.N. Luckyanova, J. Garg, K. Esfarjani, A. Jandl, M.T. Bulsara, A.J. Schmidt, A.J. Minnich, S. Chen, M.S. Dresselhaus, Z. Ren, E.A. Fitzgerald, G. Chen, Coherent phonon heat conduction in superlattices, Science 338 (2012) 936.
[21] J.-K. Yu, S. Mitrovic, D. Tham, J. Varghese, J.R. Heath, Reduction of thermal conductivity in phononic nanomesh structures, Nat. Nanotechnol. 5 (2010) 718.
[22] B.L. Davis, M.I. Hussein, Nanophononic metamaterial: thermal conductivity reduction by local resonance, Phys. Rev. Lett. 112 (2014): 055505.
[23] S. Hu, S. Ju, C. Shao, J. Guo, B. Xu, M. Ohnishi, J. Shiomi, Ultimate impedance of coherent heat conduction in van Der waals graphene-MoS2 heterostructures, Mater. Today Phys. 16 (2021) 100324.
[24] N. Yazdani, T. Nguyen-Thanh, M. Yarema, W.M.M. Lin, R. Gao, O. Yarema, A. Bosak, V. Wood, Measuring the vibrational density of states of nanocrystal-based thin films with inelastic X-ray scattering, J. Phys. Chem. Lett. 9 (2018) 1561.
[25] N. Yazdani, M. Jansen, D. Bozyigit, W.M.M. Lin, S. Volk, O. Yarema, M. Yarema, F. Juranyi, S.D. Huber, V. Wood, Nanocrystal superlattices as phonon-engineered solids and acoustic metamaterials, Nat. Commun. 10 (2019) 1.
[26] A.J. Mork, E.M.Y. Lee, N.S. Dahod, A.P. Willard, W.A. Tisdale, Modulation of low-frequency acoustic vibrations in semiconductor nanocrystals through choice of surface ligand, J. Phys. Chem. Lett. 7 (2016) 4213.
[27] L. Lindsay, First principles peierls-Boltzmann phonon thermal transport: a topical review, Nanoscale Microscale Thermophys. Eng. 20 (2016) 67.
[28] A.J.H. McGaughey, A. Jain, H.-Y. Kim, B. Fu (傅博), Phonon properties and thermal conductivity from first principles, lattice dynamics, and the Boltzmann transport equation, J. Appl. Phys. 125 (2019): 011101.
[29] X. Gu, Z. Fan, H. Bao, Thermal conductivity prediction by atomistic simulation methods: recent advances and detailed comparison, J. Appl. Phys. 130 (2021) 210902.
[30] M.T. Dove, M.T. Dove, Introduction to Lattice Dynamics, vol. 4, Cambridge university press, 1993.
[31] M. Simkin, G. Mahan, Minimum thermal conductivity of superlattices, Phys. Rev. Lett. 84 (2000) 927.
[32] M.B. Zanjani, J.R. Lukes, Phonon dispersion and thermal conductivity of nanocrystal superlattices using three-dimensional atomistic models, J. Appl. Phys. 115 (2014) 143515.
[33] R.J. Bell, P. Dean, Atomic vibrations in vitreous silica, Discuss. Faraday Soc. 50 (1970) 55.
[34] J.L. Feldman, P.B. Allen, S.R. Bickham, Numerical study of low-frequency vibrations in amorphous silicon, Phys. Rev. B 59 (1999) 3551.
[35] R. Hu, S. Iwamoto, L. Feng, S. Ju, S. Hu, M. Ohnishi, N. Nagai, K. Hirakawa, J. Shiomi, Machine-learning-optimized aperiodic superlattice minimizes coherent phonon heat conduction, Phys. Rev. X 10 (2020): 021050.
[36] J. Shiomi, S. Maruyama, Non-fourier heat conduction in a single-walled carbon nanotube: classical molecular dynamics simulations, Phys. Rev. B 73 (2006) 205420.
[37] J.A. Thomas, J.E. Turney, R.M. Iutzi, C.H. Amon, A.J.H. McGaughey, Predicting phonon dispersion relations and lifetimes from the spectral energy density, Phys. Rev. B 81 (2010): 081411.
[38] J. Liu, K. Enomoto, K. Takeda, D. Inoue, Y.-J. Pu, Simple cubic self-assembly of PbS quantum dots by finely controlled ligand removal through gel permeation chromatography, Chem. Sci. 12 (2021) 10354.
[39] P. Podsiadlo, G. Krylova, B. Lee, K. Critchley, D.J. Gosztola, D.V. Talapin, P.D. Ashby, E.V. Shevchenko, The role of order, nanocrystal size, and capping ligands in the collective mechanical response of three-dimensional nanocrystal solids, J. Am. Chem. Soc. 132 (2010) 8953.
[40] B. Qiu, H. Bao, G. Zhang, Y. Wu, X. Ruan, Molecular dynamics simulations of lattice thermal conductivity and spectral phonon mean free path of PbTe: bulk and nanostructures, Comput. Mater. Sci. 53 (2012) 278.
[41] Y. Wang, B. Qiu, A.J. McGaughey, X. Ruan, X. Xu, Mode-wise thermal conductivity of bismuth telluride, J. Heat Tran. 135 (2013): 091102.
[42] C. Shao, H. Bao, Mode-Resolved Thermal Conductivity of Freestanding and Supported Bismuth Telluride Quintuple Layer, 2016. V002T11A012.
[43] M. Jansen, N. Yazdani, V. Wood, Phonon-engineered solids constructed from nanocrystals, Apl. Mater. 7 (2019): 081124.
[44] S.M. Sadat, R.Y. Wang, Colloidal nanocrystal superlattices as phononic crystals: plane wave expansion modeling of phonon band structure, RSC Adv. 6 (2016) 44578.
[45] Y. Hu, S. Li, H. Bao, First-principles based analysis of thermal transport in metallic nanostructures: size effect and wiedemann-franz law, Phys. Rev. B 103 (2021) 104301.
[46] J. Xu, Y. Hu, X. Ruan, X. Wang, T. Feng, H. Bao, Nonequilibrium phonon transport induced by finite sizes: effect of phonon-phonon coupling, Phys. Rev. B 104 (2021) 104310.
[47] R. Clasen, P. Grosse, A. Krost, F. Levy, S.F. Marenkin, W. Richter, N. Ringelstein, R. Schmechel, G. Weiser, H. Werheit, Non-tetrahedrally bonded elements and binary compounds I, Landolt-Bornstein New Ser. Group III **17** (1998).
[48] Z. Wang, X. Ruan, On the domain size effect of thermal conductivities from equilibrium and nonequilibrium molecular dynamics simulations, J. Appl. Phys. 121 (2017): 044301.
[49] H. Wei, H. Bao, X. Ruan, Genetic algorithm-driven discovery of unexpected thermal conductivity enhancement by disorder, Nano Energy 71 (2020) 104619.
[50] S. Hu, L. Feng, C. Shao, I.A. Strelnikov, Y.A. Kosevich, J. Shiomi, Two-path phonon interference resonance induces a stop band in a silicon crystal matrix with a multilayer array of embedded nanoparticles, Phys. Rev. B 102 (2020): 024301.
[51] D. Jishkariani, K.C. Elbert, Y. Wu, J.D. Lee, M. Hermes, D. Wang, A. van Blaaderen, C.B. Murray, Nanocrystal core size and shape substitutional doping and underlying crystalline order in nanocrystal superlattices, ACS Nano 13 (2019) 5712.
[52] Z. Fan, R.S. Koster, S. Wang, C. Fang, A.O. Yalcin, F.D. Tichelaar, H.W. Zandbergen, M.A. van Huis, T.J.H. Vlugt, A transferable force field for CdS-CdSe-PbS-PbSe solid systems, J. Chem. Phys. 141 (2014) 244503.
[53] W.-L. Ong, S. Majumdar, J.A. Malen, A.J.H. McGaughey, Coupling of organic and inorganic vibrational states and their thermal transport in nanocrystal arrays, J. Phys. Chem. C 118 (2014) 7288.
[54] T. Luo, J.R. Lloyd, Equilibrium molecular dynamics study of lattice thermal conductivity/conductance of Au-sam-Au junctions, J. Heat Tran. 132 (2010): 032401.
[55] C.J. Fennell, J.D. Gezelter, Is the ewald summation still necessary? Pairwise alternatives to the accepted standard for long-range electrostatics, J. Chem. Phys. 124 (2006) 234104.
[56] C.R. Bealing, W.J. Baumgardner, J.J. Choi, T. Hanrath, R.G. Hennig, Predicting nanocrystal shape through consideration of surface-ligand interactions, ACS Nano 6 (2012) 2118.
[57] R. Li, K. Bian, T. Hanrath, W.A. Bassett, Z. Wang, Decoding the superlattice and interface structure of truncate PbS nanocrystal-assembled supercrystal and

associated interaction forces, J. Am. Chem. Soc. 136 (2014) 12047.
[58] T. Tadano, Y. Gohda, S. Tsuneyuki, Anharmonic force constants extracted from first-principles molecular dynamics: applications to heat transfer simulations, J. Phys. Condens. Matter 26 (2014) 225402.
[59] K. Sääskilahti, J. Oksanen, J. Tulkki, S. Volz, Spectral mapping of heat transfer mechanisms at liquid-solid interfaces, Phys. Rev. E 93 (2016): 052141.
[60] A.P. Thompson, H.M. Aktulga, R. Berger, D.S. Bolintineanu, W.M. Brown, P.S. Crozier, P.J. in 't Veld, A. Kohlmeyer, S.G. Moore, T.D. Nguyen, R. Shan, M.J. Stevens, J. Tranchida, C. Trott, S.J. Plimpton, Lammps - a flexible simulation tool for particle-based materials modeling at the atomic, meso, and continuum scales, Comput. Phys. Commun. 271 (2022) 108171.